High Power Laser Science and Engineering, (2025), Vol. 13, e50, 13 pages.
doi:10.1017/hpl.2025.35

HIGH POWER LASER SCIENCE AND ENGINEERING

RESEARCH ARTICLE

Definite vacuum for strong-field quantum electrodynamics experiments

Qiqi Yu[1,2,3], Baifei Shen[3], Stefan Bock[1], Ulrich Schramm[1,4], Thomas E. Cowan[1,4], Roland Sauerbrey[1,4], and Hans-Peter Schlenvoigt[1]

[1]*Helmholtz-Zentrum Dresden – Rossendorf, Dresden, Germany*

[2]*Qingdao University of Technology, Qingdao, China*

[3]*Shanghai Normal University, Shanghai, China*

[4]*TUD Dresden University of Technology, Dresden, Germany*

(Received 30 October 2024; revised 15 February 2025; accepted 9 April 2025)

Abstract

Ultra-intense lasers can generate the strongest electromagnetic fields in laboratory conditions, and are expected to perform tests of quantum electrodynamics (QED) in yet unexplored parameter ranges. Such experiments require knowledge of the field strengths and all possible interaction pathways. The latter can be simplified if a perfect, particle-free vacuum is present, thereby excluding competing interactions. We propose a method to evacuate all residual gas particles prior to QED interactions, based on tunnel ionization by a preceding auxiliary laser pulse and a static electric field. We present modelling and experimental results of testing this method on a 0.5 TW chirped pulse amplification laser system. Experimental results match well the simulations for the given conditions and thereby provide valuable understanding to extrapolate this method for QED experiments with PW-class laser systems where it can likewise be employed for *in situ* peak field strength characterization.

Keywords: strong-field quantum electrodynamics; time-of-flight spectroscopy; tunnel ionization; vacuum generation

1. Introduction

Since the advent of ultra-intense lasers[1–4], electric/magnetic fields of unprecedented magnitudes have been available in laboratories. For laser intensities above 10^{22} W/cm^2, electric fields exceed 10^{16} V/m where features of radiation reaction, vacuum-polarization, pair production and quantum electrodynamics (QED) cascades are predicted[5]. Many proposals have been published for studying the interaction of ultra-intense fields with vacuum[6–11]. However, the outcomes of such planned experiments depend on (i) attaining the relevant field strengths in the laser focus and (ii) suppressing any background effect that could make the outcome ambiguous. Obst-Huebl *et al.*[12] highlighted how severely laser-generated proton beams can be affected by electric fields from residual gas ionization far off the laser focus. Since strong-field QED experiments require peak intensities of the order of 10^{23} W/cm^2, residual gas ionization can occur in larger volumes and to high-charge states, and therefore must be considered in strong-field QED experiments.

Characterizing the laser focus intensity *in situ* is a challenge and of particular importance for strong-field QED experiments[13–19]. A widely studied method[20] relies on the dependency of the attainable ion charge state by tunnel ionization on the laser electric peak field. After ionization by the short, ultra-intense laser pulse, ions are accelerated in an external static electric field, such that different species are separated temporally due to the charge-to-mass-ratio (q/m) dependency of the acceleration, and can be ultimately identified with a time-of-flight (ToF) setup. Recent conceptual studies suggest[13–16] that this method is reliable for intensities between 10^{20} and 10^{24} W/cm^2.

Other methods to directly infer laser peak intensity, thus avoiding considerable laser–plasma interactions, often utilize electron dynamics and either detect emitted radiation or electron momenta. Ponderomotive scattering of plasma electrons[21,22] or detection of emitted radiation[23,24] generally applies to modest peak intensities of less than 10^{21} W/cm^2 since electrons are quite light and thus are expelled from peak-intensity regions before the laser

Correspondence to: H.-P. Schlenvoigt, Helmholtz-Zentrum Dresden – Rossendorf, 01328 Dresden, Germany. Email: hp.schlenvoigt@hzdr.de

pulse maximum is reached. Reverting to relativistic electrons (nonlinear Thomson scattering or inverse Compton scattering)[25,26] ensures that they can stay on the laser axis to witness laser peak intensity, but realization is inconvenient due to the need for a well-controlled electron accelerator. An interesting idea[27] couples tunnel ionization from noble gas atoms, subsequent electron dynamics and radiation emission, and ultimately Breit–Wheeler pair production, as a chain of processes to infer laser peak intensity. That method is said to be relevant above 10^{23} W/cm^2, but also highlights the need for a particle-free vacuum as it relies on a QED process.

We propose to employ the same experimental arrangement of a static electric field as in Ref. [20] in conjunction with an additional, preceding, lower-power fs pulse, to provide a transient particle-free region (void) around the main laser focus, excluding competing effects from residual gas particles[9]. Thus, the same apparatus can be used for both characterizing the main laser pulse (driving the QED experiments) and providing controlled, clean vacuum conditions for QED interactions, allowing for conclusive, unambiguous interpretations.

The proposed method is depicted in Figure 1. It employs for cleaning a lower-power (a few tens of mJ to 100 mJ) and small diameter (few mm) laser pulse to ionize a large region around the main pulse focus. This can be easily achieved with a collinear beam, using the same final focusing optics. Consequently, a large (100 μm) volume of ions (and electrons, not shown) is generated around the location of the main beam focus (few μm). The static external electric field evacuates the charged particles from that region within a time determined by the field strength and region diameter. Then, with a certain delay τ to the first pulse (a few tens of ns), the main pulse can arrive in that void and interactions with real particles cannot happen.

Since thermal motion of residual gas and ions is present (indicated by dashed arrows), volumes of void and ions are dynamic. Thermal velocities at room temperature are of the order of 1000 m/s; thus, a void of 100 μm size is refilled with residual gas particles on timescales of 100 ns. Eventually, the void vanishes and the average vacuum conditions are recovered.

This concept is relevant for high-power laser QED experiments since typical (thermodynamic equilibrium) vacuum conditions are at the lower end of high vacuum (HV), 10^{-6} mbar or above. The probability to encounter a gas particle per 1 μm^3 volume is about 1/40 or higher, being much more frequent than the probability for a QED event. Reaching ultra-high vacuum (UHV) conditions would require bake-out, which will temporarily induce mechanical stress to mounted optics due to different thermal expansion coefficients of optics material (glass) and mounting material (metals). Bake-out would comprise both the experimental chamber as well as the pulse compression chamber, posing a significant risk for pulse compression, beam propagation and alignment.

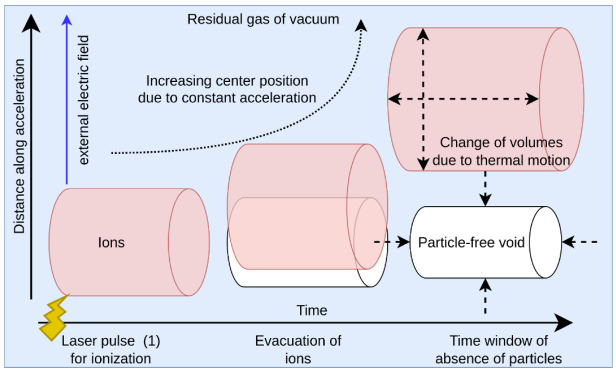

Figure 1. Drawing of the principle of generating a particle-free, transient void in a vacuum atmosphere. A laser pulse converts all residual gas (blue) within a certain volume into ions (red). A constant, externally applied electric field accelerates the ions in one direction. If that happens fast enough compared to the thermal motion (indicated by dashed arrows), a void (white) can be generated.

This paper presents a test study of that 'cleaning' method. A 0.5 TW chirped pulse amplification (CPA) laser system was employed, able to achieve intensities of up to 10^{16} W/cm^2. It was modified to generate two pulses with defined delay τ. The second pulse, having a larger beam diameter and more energy than the first pulse, was focused to higher intensities and a smaller waist but to the same location as the first one in order to probe whether there were still ions present: if so, it would ionize them to higher charge states than those at which they were already excited by the first pulse, being a clear signature of an interaction of the second pulse with particles in its focus. Ion species distributions were recorded by a ToF detector. For correct pulse timing τ, occurrence of highly charged ions ceased, in agreement with simulations for the experimental parameters.

2. Methods

2.1. Experimental setup

The experiment utilized a 0.5 TW titanium:sapphire CPA laser system at 800 nm centre wavelength, based on a mode-locked oscillator, grating stretcher, fibre transport to a regenerative amplifier followed by a six-pass amplifier in free propagation. The amplifiers delivered ca. 25 mJ in a 3 mm diameter beam and s-polarization at 10 Hz repetition rate. The beam diameter was then increased by a Galilei-type 4× beam expander to reduce the fluence and provide better beam propagation.

Then a split-and-delay unit (SDU) follows to create two pulses with (i) variable delay, (ii) variable energy ratio and (iii) different beam sizes. The schematic of the SDU is shown in Figure 2. A rotatable λ/2 waveplate combined with

https://doi.org/10.1017/hpl.2025.35 Published online by Cambridge University Press

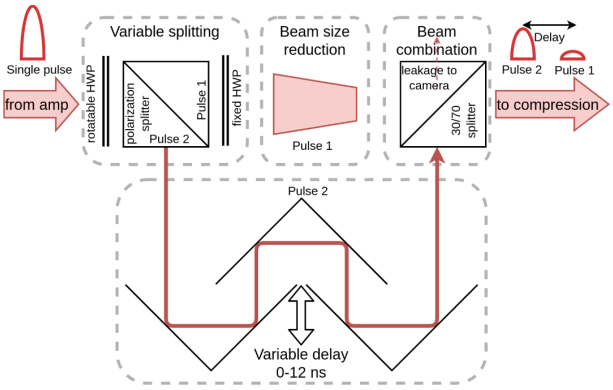

Figure 2. Schematic of the split-and-delay unit (SDU).

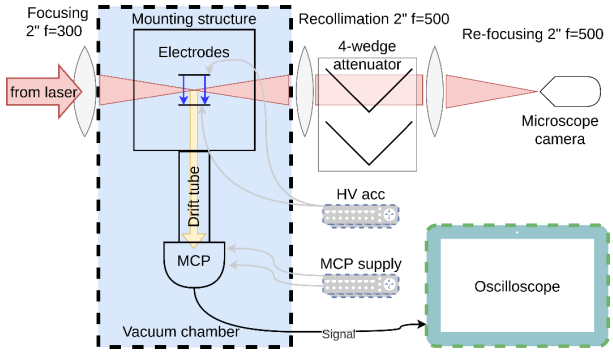

Figure 3. Schematic of the experimental setup.

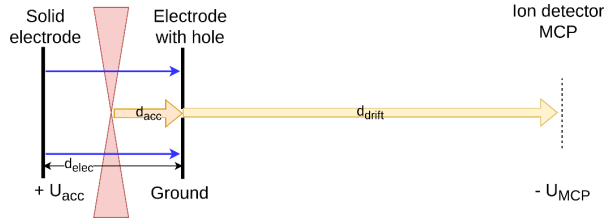

Figure 4. Schematic of the ToF setup.

a polarization beamsplitter was used to split the laser pulses with arbitrary splitting ratios and without losses. A fixed $\lambda/2$ waveplate was set in the path of the undelayed pulse (pulse 1) to have both pulses in the same polarization. Pulse 2 followed a variable delay path, employing retro-reflector mirrors in two passes, allowing for delays up to $\tau = 12$ ns on a 1 m sliding rail. Pulse 1 followed a propagation distance to match the zero delay distance of pulse 2 (not shown) and a beam size reduction by a Galilei-type 2× beam expander in reverse. The beam paths were recombined by a non-polarizing 30:70 plate beamsplitter (to sustain the increased fluence in beam 1). It was oriented such that pulse 2 was transmitted with 70% and pulse 1 reflected with 30% relative energy. The parasitic path (70% of pulse 1 and 30% of pulse 2) was used for a near-field diagnostic and a far-field diagnostic to ensure overlap and collinearity of both beams when changing the delay of pulse 2. The near-field diagnostic was also employed to find the zero delay position by visible interference fringes. After overlapping, the pulses were sent into a grating pulse compressor (70% transmission).

Laser pulse diagnostics could be inserted into the beam path after laser pulse compression: a Wizzler device to measure and optimize temporal pulse compression and a laser energy meter to measure pulse energy. Pulse duration was determined to be $\tau_{1/2} \approx 55$ fs and was not changed during experiments. Pulse energies were varied by the adjustable waveplate; see above and Section 3.1.1.

After compression and invasive diagnostics followed ca. 2 m propagation to the interaction chamber, which is shown in Figure 3. The pulses were focused by an $f = 300$ mm achromatic lens into a vacuum chamber with pressure of ca. 7×10^{-7} mbar, achieved by a turbo pump and scroll pump. After passing through the chamber the beams were re-collimated, attenuated by a reflective attenuator assembly and focused again, now in air but below the ionization threshold, by $f = 500$ mm achromatic lenses. That provided a replica of the in-vacuum focus, which was finally observed by a camera microscope (Mitutoyo 10×APO and 160 mm tube length). That was a crucial online diagnostic for the spatial overlap of the foci in vacuum, not achievable with the far-field diagnostic before the pulse compression. Focus waists were measured as $w_1 = 40$ µm and $w_2 = 30$ µm, in reasonable agreement with the beam diameter ratio and absolute beam sizes. Combined with pulse duration and pulse energy, intensities in the range of 10^{14}–10^{16} W/cm^2 were attainable.

The vacuum chamber housed the electrode assembly, providing the static external electric field (shown in pink) to evacuate the ions out of the focus, and the ToF ion detection by means of a micro-channel plate (MCP) detector after a $d_{drift} = 30$ cm long drift distance for species separation, cf. Figure 4. The electrodes had 20 mm diameter and $d_{elec} = 4$ mm distance. The left-hand electrode held positive potential U_{acc}, accelerating ions towards the right-hand electrode (on the ground). A 1 mm diameter hole in the right-hand electrode allowed for ions from the focus centre entering the drift region towards the MCP (on potential $-U_{MCP}$, slightly accelerating further) but blocked ions from regions of low intensity off centre. The Rayleigh lengths for the above-mentioned waists are approximately equal to 5 mm; thus, low-intensity regions are quite long and thus would have generated a large number of ions of low charge, not relevant for this study. The focus was aligned relative to the hole and in the middle between the electrodes, such that $d_{acc} \approx 0.5 d_{elec} = 2$ mm. The latter determines the starting position within the electric potential, and thus the attainable kinetic energy and hence the ToF time.

For the sections and voltages as depicted in Figure 4, the ToF time may be calculated as given by Equation (1), where

https://doi.org/10.1017/hpl.2025.35 Published online by Cambridge University Press

amu is the atomic mass unit, e_0 the elementary charge, A is the ion's mass number and Z is its charge:

$$T_{\mathrm{ToF}} = \sqrt{\frac{2\ \mathrm{amu}}{e_0}}\sqrt{\frac{A}{Z}} \times \left[\sqrt{\frac{d_{\mathrm{acc}}}{U_{\mathrm{acc}}/d_{\mathrm{elec}}}} + \sqrt{\frac{U_{\mathrm{acc}} d_{\mathrm{acc}} d_{\mathrm{drift}}^2}{U_{\mathrm{MCP}}^2 d_{\mathrm{elec}}}}\left(\sqrt{1+\frac{U_{\mathrm{MCP}} d_{\mathrm{elec}}}{U_{\mathrm{acc}} d_{\mathrm{acc}}}} - 1\right)\right]. \quad (1)$$

One can show that the fastest species with $A/Z = 1$, being hydrogen ions, take several hundred nanoseconds. Molecule ions from species in air can have $A/Z \sim 30$ and therefore take up to ca. six times longer, on the microsecond scale. Thus, ion detection requires a time resolution of about 100 ns (at a full range of about 10 µs) in order to discriminate the ion species. To further identify which of the pulses generated certain ions, 1 ns time resolution would be required, which was not available. Thus, the pulse identification must be done by differential measurements of pulse 1 only, pulse 2 only and pulses 1 and 2 combined in order to reveal the void generation by absence of particles for the second pulse at specific conditions.

2.2. *Experiment design*

For preparation and detailed design of the experiment, two simulation suites were developed. One modelled quantitatively the ionization of residual gas by a focused and pulsed Gaussian beam in three dimensions, providing charge state probability density distributions. The second one modelled the evolution of initially cylindrical volumes of ideal gas, as shown in Figure 1, under the action of an external electric field and finite temperature, and computed the number of particles in a second cylindrical volume as a function of time.

The first simulation modelled the focus laser intensity distribution in space and time $I(x,y,z,t)$ as a product of a purely spatial and a purely temporal dependency, as follows:

$$I(x,y,z,t) = I_0 \times \mathcal{I}(r,z) \times \tilde{I}(t). \quad (2)$$

The spatial dependency was modelled as a Gaussian beam $\mathcal{I}(r,z)$ in cylindrical symmetry coordinates $r = \sqrt{x^2+y^2}, z$, where the longitudinal coordinate z is the beam propagation axis. It took as input the laser pulse wavelength λ, the Gaussian beam waist before focusing w_{beam} and the focal length f, as follows:

$$\mathcal{I}(r,z) = \frac{1}{1+z^2/z_{\mathrm{R}}^2}\exp\left(-2\frac{r^2}{w^2(z)}\right), \quad (3a)$$

$$w(z) = w_0\sqrt{1+z^2/z_{\mathrm{R}}^2}, \quad (3b)$$

$$z_{\mathrm{R}} = \pi w_0^2/\lambda, \quad (3c)$$

$$w_0 = \lambda f/(\pi w_{\mathrm{beam}}). \quad (3d)$$

The temporal dependency $\tilde{I}(t)$ was modelled as a Gaussian pulse, characterized by a full width at half maximum (FWHM) pulse duration $\tau_{1/2}$, as follows:

$$\tilde{I}(t) = \exp\left[(\ln 0.5)\, t^2/\tau_{1/2}^2\right]. \quad (4)$$

All shape functions were maximum-normalized, such that a single factor I_0, the peak intensity in focus $r = z = 0$ and temporal maximum $t = 0$ could be employed. To relate I_0 to the pulse energy W_{L}, integration over space and time was employed.

In a second step, the generation of ions from the residual gas species (N_2, O_2, H_2O) was computed by the numerical modelling[28] of tunnel ionization[29,30] included in PICon-GPU[31] (not the full PIC suite), using the respective ionization potentials of molecular and atomic ions from the National Institute of Standards and Technology (NIST)[32] and employing both the temporal intensity envelope $\tilde{I}(t)$ and the peak-intensity I_0 for linear polarization. For the remainder, we consider only the resulting ionization (after the laser pulse is over) and introduce the local peak intensity:

$$\widehat{I}(r,z) = I_0 \times \mathcal{I}(r,z). \quad (5)$$

A result from this step for $\lambda = 800$ nm and $\tau_{1/2} = 55$ fs is shown in Figure 5. It displays the probability for ion species (different charge states) from nitrogen and oxygen, N^{1+}, N^{2+}, etc., and O^{1+}, O^{2+} etc., dependent on laser peak intensity. These ions are relevant for this study since they can be altered by the second, more intense pulse by further ionization to a charge state higher than that the first pulse can produce. Ionized molecules such as N_2^+, O_2^+, H_2O^+ can occur at low intensities as well but will Coulomb-explode when being ionized further. Hydrogen ions H^+ cannot be altered.

Figure 5 shows a first mandatory condition – any pulse must exceed a threshold intensity

$$I_{\mathrm{Thr}} = 5 \times 10^{14}\ \mathrm{W/cm^2} \quad (6)$$

in order to ionize any gas particle. Here, nitrogen sets the limit to achieve a high probability for N^{1+}; O^{1+} is already at 4×10^{14} W/cm^2 and certainly ionized. This threshold intensity ensures that all gas molecules are ionized and can then be evacuated by the external electric field.

Secondly, Figure 5 also shows that for any peak intensity of pulse 1, pulse 2 must be five times more intense in order to ionize particles to a higher charge state than pulse 1, and thereby mark them as detected. Here, the value is given by

https://doi.org/10.1017/hpl.2025.35 Published online by Cambridge University Press

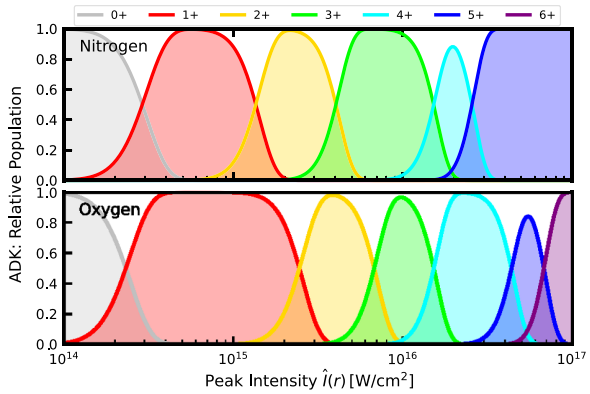

Figure 5. Model dependency of generated ion species from nitrogen and oxygen on laser peak intensity for a 55 fs Gaussian laser pulse, at the end of the laser pulse. Oxygen exhibits a relatively long interval of O^+ until further electrons become ionized.

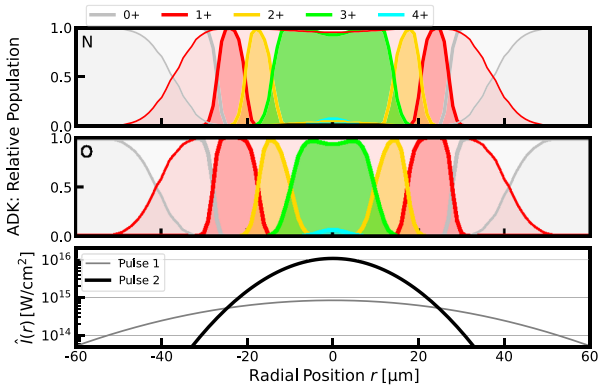

Figure 6. Simulated radial ion species distribution in focus ($z = 0$) for an ideal case: Pulse 1 is focused to 50 µm waist with 2 mJ, yielding 8.4×10^{14} W/cm^2 peak intensity; pulse 2 is focused to 20 µm waist with 4 mJ, yielding 1.1×10^{16} W/cm^2 peak intensity. The radial intensity profiles are shown in the bottom panel, pulse 1 as a thin grey line and pulse 2 as a thick black line. Above are the radial ion species distributions for nitrogen (top panel) and oxygen (centre panel). Thin lines represent distributions after pulse 1 and thick lines after pulse 2.

oxygen in order to ionize O^{1+} from pulse 1 to O^{2+} by pulse 2. This leads to a second condition:

$$\widehat{I}^{\mathrm{P2}}(r,z) > 5 \times \widehat{I}^{\mathrm{P1}}(r,z), \tag{7}$$

ensuring that species, generated by pulse 1, can be modified by pulse 2 if they are still present upon arrival of pulse 2, in order to discriminate ions from pulses 1 and 2.

Mapping the peak-intensity-dependent ion species probabilities to the local peak intensity $\widehat{I}(r,z)$ given by the spatial intensity modelling (Equation (3)), the simulation could compute for given experimental laser parameters the species-resolved probability densities in three dimensions, which can be sampled on points, lines or planes or summed over volumes.

That was done, as a second design refinement, perpendicular to the beam direction, first at $z = 0$. Figure 6 shows, for an idealized case (see caption), the radial ion distributions generated by pulse 1 (thin) and pulse 2 (thick), respectively.

Concerning the condition in Equation (6), pulse 1 ionizes the residual gas to single-charged ions N^{1+} and O^{1+} but not higher (thin lines in upper panels). Due to the spatial dependency given by Equation (5), a cleaning radius R_{clean} can be defined by inserting Equation (5) into Equation (6) and solving for r. For the example in Figure 6,

$$R_{\mathrm{clean}} \approx 30\ \mu\mathrm{m}. \tag{8}$$

Pulse 2, on the other hand, is able to generate single-, double- and triple-charged ions. Hence, a pulse-2-only signal would be very different from a pulse-1-only signal. Furthermore, ion generation by pulse 2 is restricted to a region fully contained within the region of single-charged ions from pulse 1; pulse 2 is unable to generate any ions outside the distribution from pulse 1, $r > 30$ µm. Consequently, if the single-charged ions generated by pulse 1 are evacuated by the external electric field upon arrival of pulse 2 (evacuation is not part of this simulation suite but rather another, see later), the region $0 < r < 30$ µm will contain no particles. Hence, pulse 2 cannot generate any ions in addition to those generated earlier by pulse 1, and a pulses 1 and 2 combined ion signal would be identical to a pulse-1-only signal, being evidence of the generation of the void.

However, if particles are still present, the condition in Equation (7) must be considered, which can be generalized, depending on the ion species of pulses 1 and 2: a probing radius R_{probe} can be defined where pulse 2 could generate ion species not accessible with pulse 1, given by the corresponding, species-dependent threshold intensity, yielding $R_{\mathrm{probe}}\left(\mathrm{X}^{n+}\right)$ for species X in charge state n.

In order to be able to alter ions from pulse 1 for probing but also to probe only within the cleaning region, a third condition must be fulfilled, which reads as follows:

$$0 < R_{\mathrm{probe}}\left(\mathrm{X}^{n+}\right) < R_{\mathrm{clean}}. \tag{9}$$

For actual experiments with limited alignment accuracy of both beams, this translates to an alignment margin:

$$\Delta r\left(\mathrm{X}^{n+}\right) = R_{\mathrm{clean}} - R_{\mathrm{probe}}\left(\mathrm{X}^{n+}\right). \tag{10}$$

This margin depends not only on the general focus shapes and intensities but also on the ion species under investigation.

Table 1 summarizes the respective radii from the example of Figure 6. Choosing highly charged ions as the detection channel implies a smaller region where these ions can be generated. This provides a larger alignment margin but comes at the cost of a smaller number of ions possibly generated.

https://doi.org/10.1017/hpl.2025.35 Published online by Cambridge University Press

Table 1. Radii from Figure 6 where pulse 1 can generate N^{1+} or O^{1+} (being R_{clean}) and where pulse 2 can generate higher charge states (being R_{probe}), and the respective differences as defined by Equation (9).

Species	R_{clean}	R_{probe}	Δr
N^{1+}	28 μm	–	–
N^{2+}	–	18 μm	10 μm
N^{3+}	–	13 μm	15 μm
O^{1+}	30 μm	–	–
O^{2+}	–	15 μm	15 μm
O^{3+}	–	8 μm	22 μm

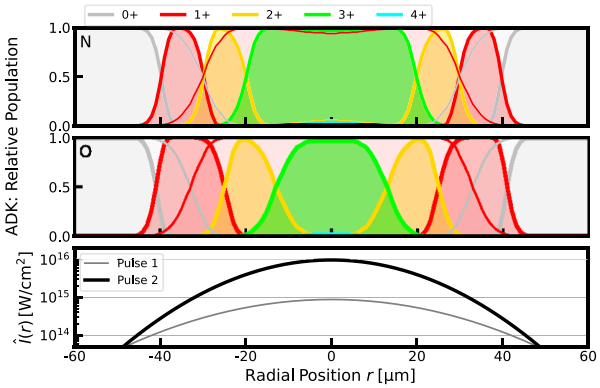

Figure 7. Simulated radial ion species distribution as in Figure 6 but for realistic conditions. Pulse 1 is focused to a 40 μm waist with 1.3 mJ, yielding 8.8×10^{14} W/cm^2 peak intensity; pulse 2 is focused to a 30 μm waist with 8 mJ, yielding 9.7×10^{15} W/cm^2 peak intensity.

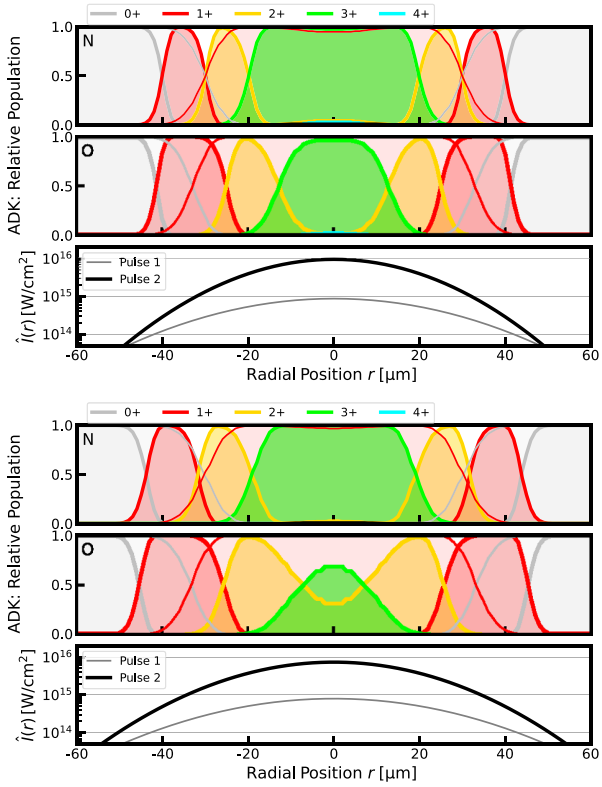

Figure 8. Simulated radial ion species distribution as in Figure 7 but out of focus at $z = 500$ μm (top) and $z = 2$ mm (bottom).

In the experimental realization, such ideal laser diameter conditions as discussed above could not be obtained. The waist ratio was 40:30 instead of 50:20, and pulse energies could not be varied independently. Most critical was that the area where pulse 2 generated the same (single-charged) species as pulse 1 was not contained within that area of pulse 1. The results for such a more realistic case are shown in Figure 7. As can be seen, the waist ratio is insufficient to prevent pulse 2 generating N^{1+} and O^{1+} ions outside where pulse 1 does so. Thus, pulse 2 will always generate those ions by ionizing residual gas, left over from pulse 1, in addition to these species generated by pulse 1. Still, N^{3+} and O^{3+} are exclusive to pulse 2, and their absence in a pulse 1 and 2 combined ion signal would indicate absence of particles and thus the generation of the void. While that is qualitatively the same as for the ideal case, the radial margin between the region of highest charged ions from pulse 2 and ionization by pulse 1 has reduced from ca. 20 μm for the ideal case to ca. 10 μm for the realistic case. This quantitative change turned out to be very critical during realization.

Figure 8 shows the radial distributions as in Figure 7 but out of focus for different positions along the beam axis. This is important because pulses 1 and 2 evolve differently along z; pulse 2 will eventually obtain a larger diameter in any case (also for the ideal case) and thus it will not be contained within pulse 1.

The experimental setup included a 1 mm diameter aperture for the ions. Thereby, only ions generated within $|z| \leq 500$ μm were detected. The distribution for that limit $z = 500$ μm is shown in the upper graph of Figure 8. There are only negligible differences to the in-focus case $z = 0$, Figure 7. The bottom graph of Figure 8 shows the distributions at $z = 2$ mm, being quantitatively different from $z = 0$ and thereby demonstrating the importance of the aperture.

The second simulation suite was used to study the trade-off between cleaning and probing radii, external field strength and pulse delay τ. It models two cylindrical volumes like in Figure 1: one for the ions generated by pulse 1 (with R_{clean}) and a second one where pulse 2 can generate the highest charge states (with R_{probe}). That is a fair approximation as the previous paragraphs have shown: species probabilities vary steeply in the radial direction and are very weak in the longitudinal direction. The simulation models the time dependence of the particle probability density (i) for an initially cylindrical low-Z ion distribution under the influence of both an external electric field and thermal motion and (ii) for the remaining volume of residual gas (inverse cylinder) with thermal motion only, cf. Figure 1. Coulomb repulsion of ions is not considered. It yields, as a function of time,

https://doi.org/10.1017/hpl.2025.35 Published online by Cambridge University Press

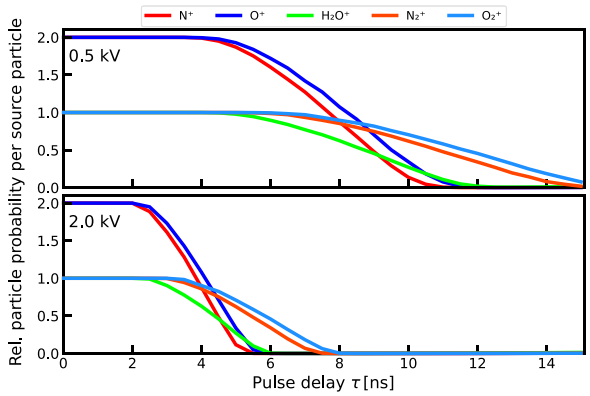

Figure 9. (Simulation) Time dependence of low-Z ions, generated by pulse 1 and accelerated transversely by the static electric field (low and high voltage), counted within the probing volume relative to the initial number of gas molecules. Volume dimensions are as in Figure 6, $R_{\text{clean}} = 30\ \mu\text{m}$ and $R_{\text{probe}} = 20\ \mu\text{m}$.

the number of particles (either ions or neutral molecules) expected to be found inside the second cylindrical volume of length $L_{\text{probe}} = 1$ mm (and $L_{\text{clean}} \gg L_{\text{probe}}$), representing the region where pulse 2 can generate specific ions. The radii, temperature, particle masses, charge state and electric field play a role.

Figure 9 displays the simulation results for low and high acceleration voltage and for further parameters as described earlier ($d_{\text{elec}} = 4$ mm, $R_{\text{clean}} = 30\ \mu\text{m}$ and $R_{\text{probe}} = 20\ \mu\text{m}$). It shows the particle numbers of single-charged ($Z = 1$) atomic or molecular ions created by pulse 1 within the volume where pulse 2 could generate higher charge states, relative to the source molecule density.

For a few nanoseconds, there is no change of number because the volume where particles are counted is smaller than the original volume of particles. Please note factor 2 for atomic ions that originate from di-atomic gas molecules. Then, after a time of a few ns, the numbers decrease, faster with higher acceleration voltage. This is the result of the evacuation of ions due to the external electric field. Separations by ion masses are visible. At late times in the shown time window, a slight increase is visible as a result of thermal motion of the residual gas molecules, filling up the void, which leads to a temperature dependence. In the experiment, delays of up to $\tau = 12$ ns were available, requiring voltages of at least 1 kV according to this simulation.

Further information from the second simulation suite is the absolute number of particles, since it used not only the temperature to derive the mean particle velocity but also the pressure to infer actual numbers instead of probabilities.

The number of ions depends on the pulse ionization volume $V = \pi R^2 L$, with L being the cylinder length, vacuum pressure p, n_0 the particle density per unit pressure (e.g., $n_0 \approx 2.5 \times 10^4\ \mu\text{m}^{-3}/\text{mbar}$), q the relative contribution of the source species to the residual gas and M the number of ions that can be generated from a source species (e.g., $M = 2$ for N^{n+} from N_2), and is given by the following:

$$N = Mqn_0pV. \tag{11}$$

For a pressure of 10^{-6} mbar and a length of 1 mm (limited by the aperture in the electrode), about 7×10^4 gas particles can be ionized by pulse 1 with $R_{\text{clean}} = 30\ \mu\text{m}$. Pulse 2 should certainly dissociate any original particles ($M = 2$) and thus still generate 6×10^4 ions for $R_{\text{probe}} = 20\ \mu\text{m}$.

3. Results

3.1. Setup characterization

3.1.1. Optical setup

The key to ion detection (and detecting their absence) is proper adjustment of the laser pulses in terms of their respective spatial intensity distributions, Equation (5), and their mutual overlap, Equation (10). For intensity characterization, pulse energy, pulse duration and focus relay imaging were combined.

Pulse energies were varied in a coupled manner by the variable waveplate before the beam splitting (see Figure 2). We used four different settings (10°, 15°, 20°, 25°), changing both pulse 1 and pulse 2 energies. For pulse 1 only and pulse 2 only, focus intensity distribution analysis was done (using pulse energy W_{L} and pulse duration $\tau_{1/2}$), yielding peak-intensity value, FWHM and $1/e^2$ areas. The results are listed in Table 2. The waveplate angle determined mainly pulse energies, and to a minor extent also the apparent focus waists. With increasing waveplate angle, the energy of pulse 1 was increasing whereas the energy of pulse 2 was decreasing. The range of settings ensured that pulse 1 was always intense enough to generate ions (cf. Equation (6), condition 1) and pulse 2 was always more intense than pulse 1 by a factor 3–20 (cf. Equation (7), condition 2). However, that condition was not satisfied for the 25° waveplate angle.

3.1.2. ToF ion detection

Investigations started with single pulse operation, either pulse 1 only or pulse 2 only. Figure 10 shows the time-resolved MCP ion detector signal as a composite graph of pulse 1 (low intensity, purple) and pulse 2 (high intensity, orange) for a 15° waveplate angle. Ion species appear as signal peaks at specific times but are followed by some electrical ringing.

Most important for analysis was the assignment of ion charge states to the peaks, since the simulations made clear that only specific high-charge states can be employed to witness the formation of a void. This assignment was realized by the dependence of ToFs on specific charge-to-mass ratios A/Z, cf. Equation (1), with $T_{\text{ToF}} \propto \sqrt{A/Z}$. Thus, plotting (not shown) each peak's ToF time versus $\sqrt{A/Z}$ for educated guesses of the ion mass A and charge state Z

https://doi.org/10.1017/hpl.2025.35 Published online by Cambridge University Press

Table 2. Results of pulse energy measurements and focus analysis for the four employed waveplate settings and either pulse 1 or pulse 2, here for a $\tau = 3$ ns optical delay path. Data for other delays are similar.

Waveplate angle	10°	15°	20°	25°
w_0^{P1}	31.8 µm	32.7 µm	35.5 µm	39.2 µm
W_L^{P1}	0.6 mJ	1.3 mJ	2.3 mJ	3.2 mJ
I_0^{P1}	6×10^{14} W/cm^2	1.3×10^{15} W/cm^2	1.9×10^{15} W/cm^2	2.2×10^{15} W/cm^2
w_0^{P2}	29.2 µm	28.0 µm	26.4 µm	27.6 µm
W_L^{P2}	9.3 mJ	8.2 mJ	6.6 mJ	4.6 mJ
I_0^{P2}	1.3×10^{16} W/cm^2	1.2×10^{16} W/cm^2	1.1×10^{16} W/cm^2	7×10^{15} W/cm^2
Ratio of W_L	1 : 15	1 : 6.3	1 : 2.9	1 : 1.4
Ratio of I_0	1 : 22	1 : 10	1 : 5.5	1 : 3.2

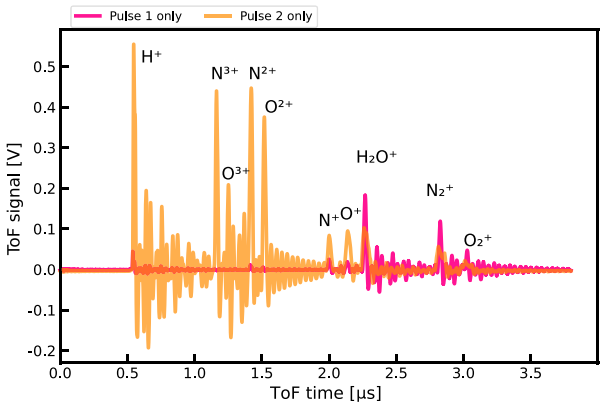

Figure 10. Measured time-of-flight ion detector traces for pulse 1 only and pulse 2 only, effectively two different laser intensities. The waveplate was set to 15°; thus, the energy ratio was 1:6, the peak-intensity ratio was ca. 1:10 and the voltage was $U_{acc} = 2$ kV.

helped to identify the species, starting here from the slowest, as molecular ions O_2^{1+}, N_2^{1+} and H_20^{1+}, followed then by atomic ions (listed here by charge state): O^{1+}, …, O^{3+}, N^{1+}, …, N^{3+} and H^+ as fastest species. These are shown as labels in Figure 10 and are first results, essential for further analysis. Also the experiment time offset relative to the external trigger was found by extrapolating $T_{ToF}\left(\sqrt{A/Z}\right)$ for $A/Z = 0$.

Further analysis used only the detector peak voltages; no ion numbers were inferred. Already the peak height reading was limited by the detector's ringing. If specific peaks might have vanished completely, the ringing may have been mistakenly read as non-zero peak height, thereby underestimating the cleaning.

Laser conditions for Figure 10 are listed in Table 2 for 15° and are close to those of Figure 7. The experimentally observed ion species agree well with predictions based on focus analysis; the peak intensity allows for ionization and dissociation of nitrogen and oxygen molecules and for ionizing the fragments mainly to the first charge state, only in the centre to the second charge state ions. Pulse 2, in contrast, was set to nine times higher intensities in order to ionize the atoms or ions further up to $Z = 3$, which was exactly what we observed. In addition, the peaks for $Z > 1$ are stronger than those for $Z = 1$, showing the stronger MCP response for ions with higher Z. In turn, that implies the number of $Z = 2$ ions from pulse 1 is indeed very small. Essentially, the conditions are chosen such that $Z = 3$ ions are exclusive to pulse 2, being one crucial condition to test the void generation.

3.1.3. *Spatial overlap*

A second requirement for void detection is the overlap of the intensity regions for cleaning and probing in space. That overlap was set by manually adjustable mirror mounts before the beam recombination of the SDU (see Figure 2). After setting the overlap, data was taken immediately to avoid drifts of the overlap. Detailed overlap analysis was done after taking all data and it revealed that the necessarily strong peak-intensity discrepancy, up to 20×, limited the precision of overlapping the peak positions during alignment (even with live image processing) and, often, the actual peak distance exceeded the margins. We refrained from altering the beam path by, for example, using neutral density filters for pulse 2, in order to not alter the apparent position on the camera, what would lead to misalignment.

Figure 11 shows composite focus images for three different waveplate settings. In each panel, the focus of beam 1 is coloured red, that of beam 2 is green, and they mix to black. For a 10° waveplate angle, beam 1 is barely visible but located to the lower right of beam 2. This is also true for the other two cases, but for 20° it is also visible in the top-left of beam 2. That means that beam 1 stretches over beam 2. Yet, the beams always have the same relative location; only their appearance is changed, demonstrating the difficulty in assessing the overlap.

However, as discussed earlier, margins are specific to peak-intensity conditions. Table 2 shows that for a 10° waveplate angle, pulse 2 is most intense and could generate the highest charge states, but pulse 1 is so weak that the area of cleaning is relatively small, limiting *per se* the alignment margin Δr. With an increasing angle, the cleaned region grows and the regions for a specific charge state as witness shrink, thus enhancing the alignment margin. On the other hand, probing volumes that are too small for a specific charge state imply that the possible number of witness ions is very small, and could be masked by the detector's ringing.

https://doi.org/10.1017/hpl.2025.35 Published online by Cambridge University Press

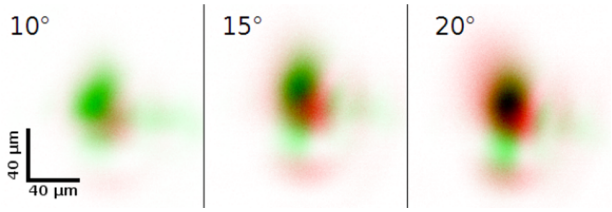

Figure 11. Series of focus composite images for the given waveplate angles (measurement). Each composite is of the same scale and shows the focus of beam 1 in red and that of beam 2 in green. At good overlap and for similar intensities, the colours mix (inversely) to black. Data are from $\tau = 9$ ns optical delay.

Table 3. Overview of experimentally realized radii for cleaning volumes and probing volumes. Here, R_{clean} is determined by $I = 3 \times 10^{14}$ W/cm^2, slightly lower than in Equation (6), R_{probe} is determined by $I = 5 \times 10^{15}$ W/cm^2 in order to generate N^{3+}, fulfilling Equation (7), and Δr is given by Equation (10) and checks for the condition in Equation (9).

Waveplate	R_{clean}	R_{probe}	Δr
10°	12.3 µm	13.3 µm	−1.0 µm
15°	17.9 µm	12.2 µm	5.7 µm
20°	22.1 µm	10.4 µm	11.8 µm
25°	25.5 µm	6.5 µm	19.0 µm

The detailed analysis processed the areal measures of focus analysis to infer a mean focus radial measure, either as the half width at half maximum (HWHM) or waist, assuming circular symmetry. With those measures and the peak intensities, relevant radii R_{clean} and $R_{\text{probe}}\left(X^{n+}\right)$ were inferred in order to calculate the allowable alignment margin Δr according to Equation (10). The intensity peak positions were used to calculate the actual alignment offset. A comparison with the allowable margin then provided information about whether cleaning should be detectable (actual peak distance less than Δr) or not, helping to select the right datasets.

Table 3 shows actual mean radii and alignment margins for the four waveplate settings. Here, R_{clean} is determined by $I^{\text{P1}} = 3 \times 10^{14}$ W/cm^2 (condition 1), slightly lower than in Equation (6), R_{probe} is determined by $I^{\text{P2}} = 5 \times 10^{15}$ W/cm^2 in order to generate N^{3+}, fulfilling Equation (7) (condition 2), and Δr is given by Equation (10) and checks for condition 3 (Equation (9)). Table 3 shows that the setting of 10° is not very promising since the cleaned region is too small and pulse 2 will always (even for perfect alignment) encounter neutral residual gas and ionize it into the highest charge state, such that no complete disappearance of ions in this state can be ever detected. Conversely, the largest waveplate angle of 25° provides ample alignment margin, but the area to generate highest charge states is quite small and thus the possible number of ions is ca. four times lower ($A \propto R^2$) than for 10°. Furthermore, the cleaning pulse was intense enough to generate $Z = 2$ ions.

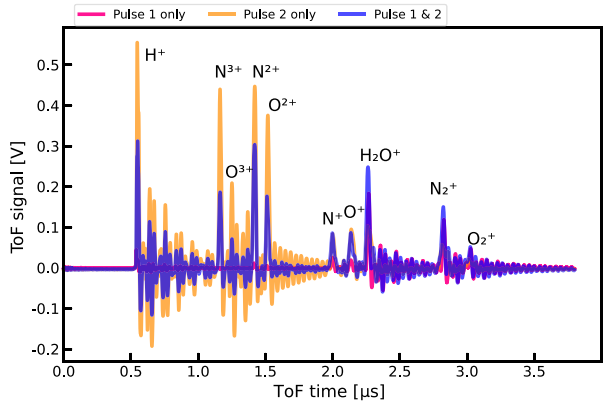

Figure 12. Measured ion signal ToF traces for the same conditions as in Figure 10, here also with the trace when both pulses were shot with $\tau = 9$ ns. As can be seen, numbers of species H^+, N^{3+}, O^{3+}, N^{2+} and O^{2+} are reduced by ca. 40%–60%.

Equation (11) allows one to calculate the possible number of ions generated with pulse 2. Here we use $p = 7 \times 10^{-6}$ mbar pressure, $L = 1$ mm (given by the hole in the electrode) and the respective values of R_{probe}; furthermore, $M = 2$ and $q = 1$ for an upper limit estimate. For 10°, up to 2×10^4 ions could be generated, but for 25° only 4.6×10^3.

3.2. *Void generation measurement*

Measurements for void generation and detection were taken for various parameters. Most central was the variation of the delay between pulses 1 and 2, where five settings were realized: $\tau \in \{0; 3; 6; 9; 12\}$ (in ns). Secondly, four different waveplate orientations were chosen ($\{10; 15; 20; 25\}$ (in deg)), providing four different energy ratios and thus four different peak intensities, as mentioned previously. Thereby, differently wide cleaning regions were realized at the cost of possibly a small number of potential witness ions. Furthermore, four different acceleration voltages were employed, $U_{\text{acc}} \in \{0.5; 1.0; 1.5; 2.0\}$ (in kV). That was done to possibly reduce the electrical ringing for peak identification. Finally, for each setting, traces of pulse 1 only, pulse 2 only and pulses 1 and 2 combined were recorded, summing up to 240 measurements where ToF traces and focus relay images were taken simultaneously. Analysis of spatial overlap showed that the overlap for $\tau = 12$ ns was not well established, thus limiting the potential for void detection at that particular delay.

An example ToF ion detector trace for void generation is shown in Figure 12. It displays the same data as Figure 10 (pink, orange) but with the additional trace (blue) when both pulses were fired with $\tau = 9$ ns delay. For that case, the number of species H^+, N^{3+}, O^{3+}, N^{2+}, O^{2+} is reduced (blue) compared to the case of pulse 2 only (orange). That means that pulse 2 encountered less oxygen or nitrogen ions when

https://doi.org/10.1017/hpl.2025.35 Published online by Cambridge University Press

pulse 1 was shot $\tau = 9$ ns earlier, because those species were already moving out of the focus region of pulse 2. The number of species N^{1+} and O^{1+} is mainly unchanged, since these species cannot witness the void formation. The number of molecular ions H_20^{1+}, N_2^{1+} and O_2^{1+} is slightly increased. These are generated at the outer areas of the focus from neutral residual gas, which moves back into the void after these species are generated by pulse 1, and thus pulse 2 can generate some more of these species, particularly at longer delays.

For further analysis, ToF traces were processed to determine for each species the peak height. Let H_1, H_2 and H_3 be the signal amplitude for pulse 1 only, pulse 2 only and pulses 1 and 2 combined, respectively, for a given species. Then, the relative height change was computed when both pulses were fired, relative to the height for pulse 2 only, as follows:

$$\Delta = \frac{H_3 - H_2}{H_2}. \tag{12}$$

If the ion peak for pulses 1 and 2 combined vanishes, $H_3 \equiv 0$, there would be 100% reduction, $\Delta = -100\%$.

Now, the relative reduction Δ for specific species as a function of pulse delay τ can be visualized for further parameters, such as acceleration voltage or waveplate setting. Figure 13 shows the relative reduction of detected species versus delay τ for the fastest acceleration $U_{\text{acc}} = 2$ kV. Several features can be recognized.

Firstly, the waveplate angle determines the transverse size of the cleaned region. For 10°, this region is relatively small because the peak intensity of pulse 1 is low. On the other hand, pulse 2 is very intense and can generate species, which are in principle able to witness the cleaning, at regions where pulse 1 was too weak and, consequently, neutral residual gas is present that is not affected by the electric field. Therefore, the variation of the number of species due to cleaning is weak, limited to 40%. Furthermore, a relatively small void can be faster re-filled with residual gas. This may explain the comeback to $\Delta = 0$ at delays larger than 6 ns.

Conversely, at 25°, the cleaned region is large and cleaning is best at the longest delay. On the other hand, the probing pulse has the weakest intensity and the possible number of highly charged ions is small. In fact, O^{3+} was almost never observed except for at $\tau = 3$ ns, where a single data point exists.

For the other waveplate configurations, conditions were between these extreme cases. Reduction of species can be observed for delays in a consistent way and was stronger than for 10°, up to 75%.

It must be noted that the traces are coded by detected species, not the evacuated species like in a simulation, cf. Figure 9. For some of the detected species, several source species are possible. For example, N^{3+} can be generated by pulse 2 from N^{2+}, N^{1+} or N_2^{1+}, depending on the actual

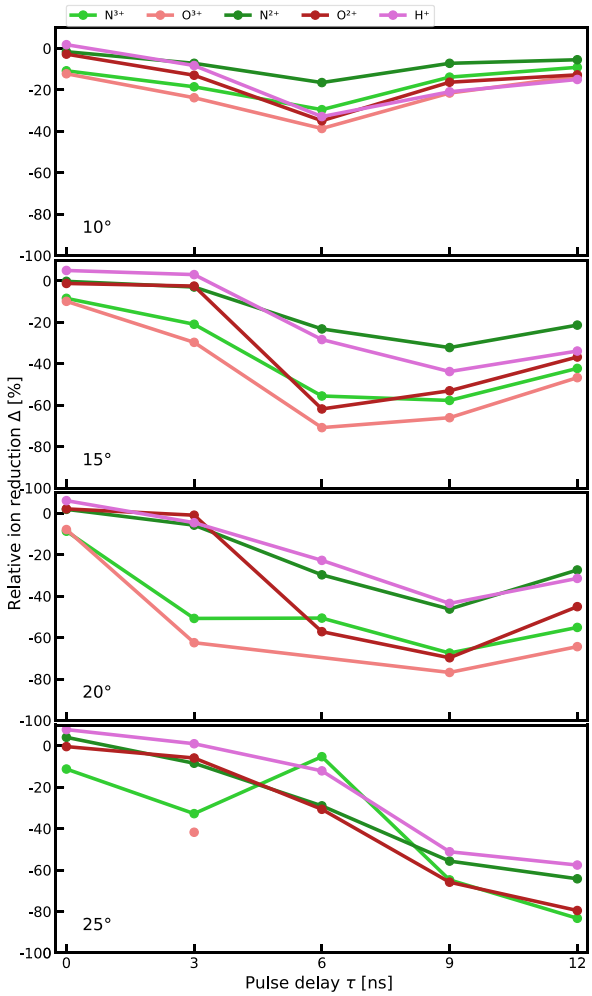

Figure 13. Relative change of peak height versus optical pulse delay, τ, for the four waveplate settings and for high acceleration voltage (measurement).

peak intensity of pulse 1. Yet, evacuation of all these different source species by the external electric field happens with different timescales due to different A/Z values. Opposite to that case is H^+, which can only originate from H_20^{1+}.

In the panel for 20° of Figure 13, we observe that the evacuation detected by N^{3+} and O^{3+} (light green and light pink) is faster than for the other displayed species. This can be explained as follows: N^{3+} as a detected species shows the average evacuation of N^{2+}, N^{1+} and N_2^{1+}, where N^{2+} leaves faster than the others. By contrast, N^{2+} as a detected species shows the average evacuation of N^{1+} and N_2^{1+}, which is the same as for the former case except for the $Z = 2$ ions.

In summary, void generation was demonstrated but not to 100% reduction, given by limitations in terms of maximum delay τ, focus diameters (determined ultimately by available laser pulse energy) and focus overlap accuracy.

https://doi.org/10.1017/hpl.2025.35 Published online by Cambridge University Press

Table 4. Quantities of the QED drive beam and for the cleaning beam, as a function of the radial fraction of the main beam. Both have 800 nm central wavelength.

Beam	QED beam	Cleaning beam ($\eta = 1\%$)[a]	Cleaning beam ($\eta = 2\%$)[a]	Cleaning beam ($\eta = 5\%$)[a]
Beam diameter D	350 mm	3.5 mm	7 mm	17.5 mm
Energy W_L	50 J	5 mJ	20 mJ	120 mJ
Pulse duration	25 fs		Same as QED beam	
Beam power P_L	2 PW	200 GW	800 GW	5 TW
Beam fluence	52 mJ/cm^2		Same as QED beam	
Beam intensity	2×10^{12} W/cm^2		Same as QED beam	
Effective waist w_{beam}	88 mm	0.88 mm	1.8 mm	4.4 mm
Beam Rayleigh length $z_{R,\,beam}$	30 km	3 m	12 m	75 m
F-number	$F/2$	$F/200$	$F/100$	$F/40$
Focus waist w_0	2 µm	200 µm	100 µm	40 µm
Focus Rayleigh length z_R	16 µm	160 mm	41 mm	6.5 mm
Focus peak intensity I_0	10^{22} W/cm^{2b}	1.5×10^{14} W/cm^2	2.5×10^{15} W/cm^2	1×10^{17} W/cm^2
Cleaning radius R_{clean}	6.2 µm	–	91 µm	66 µm

[a] η denotes the cleaning fraction of beams.
[b] Assuming 65% of the energy contained within the focus of the QED beam.

4. Outlook

Based on the successful demonstration of vacuum cleaning under limited conditions, an experiment for realistic conditions can be planned. We assume here that a QED experiment will employ a PW-scale short-pulse CPA laser to provide the strong background field. To initiate the cleaning process, we suggest that the preceding cleaning pulse is sent along the same path, utilizing the same focusing optics and thereby minimizing the setup and alignment needs. The cleaning pulse must have a smaller beam diameter (hence longer F-number) in order to obtain a focus much larger than the main beam. We further fix the incoming beam fluence (intensity) to the same value as the QED drive pulse, typically the highest reasonable value below the damage thresholds of optics, thus carrying the most energy per beam size unit. In the simplest case, the cleaning pulse could be a portion of the main beam, taking a short-cut path in order to arrive earlier.

Table 4 shows an example for a 800 nm (Ti:sapphire) QED drive laser beam of 2 PW nominal power. The beam size is chosen conservatively (large) to lower the beam fluence and intensity to 50 mJ/cm^2 and 2×10^{12} W/cm^2, respectively. A flat-top beam profile is assumed. An effective beam waist of one-quarter of the beam diameter allows one to employ Gaussian beam focusing (Equation (3)) to derive the in-focus parameters.

The three right-hand columns of Table 4 show the corresponding quantities for a cleaning beam as a function of the relative fraction in beam diameter $\eta = D_{clean}/D_{QED} < 1$. By fixing the beam fluence and pulse duration, the cleaning beam has a factor η^2 of the main pulse energy, a spot size of $1/\eta$ and a peak intensity of η^4 of the QED beam. For a QED beam reaching 10^{22} W/cm^2 and cleaning beam exceeding 5×10^{14} W/cm^2 (cf. Equation (6)), η must be of the order of a few percent. This ensures that the QED drive beam is almost unchanged when picking a small fraction for the cleaning process. In general, a smaller η provides a larger beam waist of the cleaning pulse, but it also reduces the pulse energy. The example lists for illustration that a beam with $\eta = 1\%$ is insufficient for cleaning because its peak intensity does not reach the threshold intensity are given by Equation (6), whereas larger fractions can be employed for cleaning.

Table 5. Assumed residual gas composition, based on standard atmospheric contributions, 50% relative humidity at 20°C and 70% relative pumping speed for helium (relative to nitrogen).

Contribution	Mass in a.m.u.	Rel. amount
Nitrogen	28	7.73×10^{-1}
Oxygen	32	2.07×10^{-1}
Water	18	9.90×10^{-3}
Argon	40	9.25×10^{-3}
Carbon dioxide	44	4.13×10^{-4}
Neon	20	1.80×10^{-5}
Helium	4	7.41×10^{-6}

We take for further modelling $R_{probe} = w_0 = 2$ µm and $L_{probe} = 2z_R = 32$ µm from the QED beam and for the cleaning pulse the values for $\eta = 2\%$, $R_{clean} = 90$ µm and $L_{clean} = R_{clean}$, to reduce computation efforts.

Another prerequisite is detailed knowledge about the residual gas composition, since void formation must be achieved with high reliability. Assuming that the vacuum chamber has negligible outgassing and diffusion through seals, the residual gas composition is mainly given by the ambient atmosphere via gas backstreaming. Such composition is listed in Table 5. Heavy ions limit the evacuation process since they take the longest time. This is in our case argon and carbon dioxide. For partial recovery of the average vacuum conditions by thermal motion, the lightest species are important, here helium.

Based on the geometry parameters, simulations of the evacuation and recovery process can be done, showing a time

https://doi.org/10.1017/hpl.2025.35 Published online by Cambridge University Press

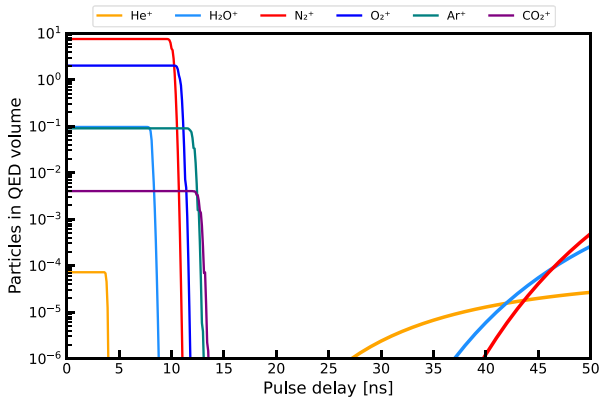

Figure 14. Simulated time dependence of the lowest-Z ions and residual gas particles, counted within the probing volume, $R_{\mathrm{probe}} = 2$ µm and $L_{\mathrm{probe}} = 32$ µm, for a backing pressure of $p = 10^{-6}$ mbar. The same external electric field strength as before, 2 kV over 4 mm electrode distance, yielding 0.5 MV/m, is employed. Thin lines are for ions, while thick lines are for uncharged gas particles.

window when a particle-free vacuum is present at the probe volume. Since the simulations model the particles with a Maxwellian velocity distribution, they yield an expectation value for the number of particles within a volume.

Here, the earlier described method was only employed for evacuation. For recovery of the average vacuum conditions at later times, computational efforts of that method became unnecessarily massive, but the geometry allowed for simple analytical modelling because the probe volume is in that case much smaller than the cleaned volume. We approximated the void as a sphere with radius R_{clean}, inscribed into the cleaned cylinder. Such a minimal void will yield a quicker re-population than the actual one, and the result will be an upper limit for the number of particles to expect at a given time. In that case, symmetry can be employed to calculate, based on a Maxwellian velocity distribution, the probability that particles from the residual gas outside the spherical void can have reached the centre.

The volume of interest, given by measures of relative peak intensity of the QED beam, is $\pi R_{\mathrm{probe}}^2 \cdot L_{\mathrm{probe}}^2 \approx 400\ \mu\mathrm{m}^3$. With the average particle density at $p = 10^{-6}$ mbar (cf. Equation (11)), the number of gas particles without cleaning is $N \approx 10$. Even with an $F/1$ focusing, reducing the volume by a factor $2^4 = 16$, about one particle would be present per shot.

Figure 14 shows how this number evolves over time, resolved by species. Until $\tau \approx 14$ ns, species evacuation takes place. It should be noted that the heavier species, despite being much less abundant, set here a limit in time. This time is also an upper limit since calculations were done for single-charged molecule ions, whereas in reality, most ions will be atomic or multiple-charged, and thus evacuated quicker.

At later times, atoms from the residual gas, outside the void, can reach the probe volume. Here, helium is important since it is the fastest species considered, even though its contribution is very small.

For experiments the gap from 15 to 25 ns is important. In that time window, the expectation value of particle count means that within 10^6 shots less than one shot with a particle in the QED focus can be expected. At laser pulse repetition rates of 10 Hz, this occurrence is equivalent to less than one false event per 24 hours. The lowest expectation value for that simulation case amounts to fewer than 10^{-11} particles at $\tau = 14.2$–14.8 ns.

For experimental realization, that time delay requires 4.5 m optical path difference. That length does not affect the beam propagation (which is shorter than the beam Rayleigh length). Due to the square-root-scaling with the accelerating electric field (cf. Equation (1)), the delays can be reduced by higher field strengths. A factor 10 increase of field strength to 5 MV/m would still be well below electrical breakdown thresholds and shorten delay times and optical paths by more than a factor of three to approximately equal to 1.5 m, being a bearable size in a typical experimental vacuum chamber.

Prospective studies of laser-based QED experiments[9,11,33–36] often provide the expected number of signal photons per shot for ideal conditions (10^{-4}–10^{-1} photons per shot) without consideration of background signals or fluctuating overlap conditions. Overall shot number estimates are rarely provided but are of the order of 10^5–10^6 shots in total for successful measurements. Therefore, our prediction of the generation of a perfect vacuum, better than 10^6 shots without a particle in a well-defined volume of 1000 µm^3 and for several tens of ns, is largely sufficient. Furthermore, the apparatus allows for *in situ* QED drive laser electric peak field characterization when the cleaning pulse is blocked and an appropriate gas, such as Xe, is added in low concentration[13].

Acknowledgements

The authors would like to thank Marco Garten for the ADK model ionization code[28] and thank Lingen Huang for fruitful discussions. The authors also would like to thank the China Scholarship Council for financial support during a visit of Qiqi Yu (File No. 201908310159) to Helmholtz-Zentrum Dresden – Rossendorf and the National Natural Science Foundation of China (Grant No. 11935008).

References

1. D. Strickland and G. Mourou, Opt. Commun. **56**, 219 (1985).
2. C. Danson, D. Hillier, N. Hopps, and D. Neely, High Power Laser Sci. Eng. **3**, e3 (2015).
3. C. N. Danson, C. Haefner, J. Bromage, T. Butcher, J.-C. F. Chanteloup, E. A. Chowdhury, A. Galvanauskas, L. A. Gizzi, J. Hein, D. I. Hillier, N. W. Hopps, Y. Kato, E. A. Khazanov, R. Kodama, G. Korn, R. Li, Y. Li, J. Limpert, J. Ma, C. H. Nam, D. Neely, D. Papadopoulos, R. R. Penman, L. Qian, J. J. Rocca, A. A. Shaykin, C. W. Siders, C. Spindloe, S. Szatmári,

https://doi.org/10.1017/hpl.2025.35 Published online by Cambridge University Press

R. M. G. M. Trines, J. Zhu, P. Zhu, and J. D. Zuegel, High Power Laser Sci. Eng. **7**, e54 (2019).
4. C. Radier, O. Chalus, M. Charbonneau, S. Thambirajah, G. Deschamps, S. David, J. Barbe, E. Etter, G. Matras, S. Ricaud, V. Leroux, C. Richard, F. Lureau, A. Baleanu, R. Banici, A. Gradinariu, C. Caldararu, C. Capiteanu, A. Naziru, B. Diaconescu, V. Iancu, R. Dabu, D. Ursescu, I. Dancus, C. A. Ur, K. A. Tanaka, and N. V. Zamfir, High Power Laser Sci. Eng. **10**, e21 (2022).
5. A. Di Piazza, C. Müller, K. Z. Hatsagortsyan, and C. H. Keitel, Rev. Mod. Phys. **84**, 1177 (2012).
6. T. Heinzl, B. Liesfeld, K.-U. Amthor, H. Schwoerer, R. Sauerbrey, and A. Wipf, Opt. Commun. **267**, 318 (2006).
7. H. Gies, Eur. Phys. J. D **55**, 311 (2009).
8. M. Marklund and J. Lundin, Eur. Phys. J. D **55**, 319 (2009).
9. H.-P. Schlenvoigt, T. Heinzl, U. Schramm, T. E. Cowan, and R. Sauerbrey, Phys. Scripta **91**, 023010 (2016).
10. N. Ahmadiniaz, T. E. Cowan, R. Sauerbrey, U. Schramm, H.-P. Schlenvoigt, and R. Schützhold, Phys. Rev. D **101**, 116019 (2020).
11. F. Karbstein, Particles **3**, 39 (2020).
12. L. Obst-Huebl, T. Ziegler, F.-E. Brack, J. Branco, M. Bussmann, T. E. Cowan, C. B. Curry, F. Fiuza, M. Garten, M. Gauthier, S. Göde, S. H. Glenzer, A. Huebl, A. Irman, J. B. Kim, T. Kluge, S. D. Kraft, F. Kroll, J. Metzkes-Ng, R. Pausch, I. Prencipe, M. Rehwald, C. Roedel, H.-P. Schlenvoigt, U. Schramm, and K. Zeil, Nat. Commun. **9**, 5292 (2018).
13. I. Ouatu, B. T. Spiers, R. Aboushelbaya, Q. Feng, M. W. Von Der Leyen, R. W. Paddock, R. Timmis, C. Ticos, K. M. Krushelnick, and P. A. Norreys, Phys. Rev. E **106**, 015205 (2022).
14. M. F. Ciappina, S. V. Popruzhenko, S. V. Bulanov, T. Ditmire, G. Korn, and S. Weber, Phys. Rev. A **99**, 043405 (2019).
15. M. F. Ciappina and S. V. Popruzhenko, Laser Phys. Lett. **17**, 025301 (2020).
16. M. F. Ciappina, E. E. Peganov, and S. V. Popruzhenko, Matter Radiat. Extremes **5**, 044401 (2020).
17. A. Yandow, T. Toncian, and T. Ditmire, Phys. Rev. A **100**, 053406 (2019).
18. O. E. Vais, A. G.R. Thomas, A. M. Maksimchuk, K. Krushelnick, and V. Yu Bychenkov, New J. Phys. **22**, 023003 (2020).
19. O. E. Vais and V. Yu Bychenkov, Plasma Phys. Control. Fusion **63**, 014002 (2020).
20. A. Link, E. A. Chowdhury, J. T. Morrison, V. M. Ovchinnikov, D. Offermann, L. Van Woerkom, R. R. Freeman, J. Pasley, E. Shipton, F. Beg, P. Rambo, J. Schwarz, M. Geissel, A. Edens, and J. L. Porter, Rev. Sci. Instrum. **77**, 10E723 (2006).
21. K. A. Ivanov, I. N. Tsymbalov, O. E. Vais, S. G. Bochkarev, R. V. Volkov, V. Yu Bychenkov, and A. B. Savel'ev, Plasma Phys. Control. Fusion **60**, 105011 (2018).
22. A. Longman, S. Ravichandran, L. Manzo, C. Z. He, R. Lera, N. McLane, M. Huault, G. Tiscareno, D. Hanggi, P. Spingola, N. Czapla, R. L. Daskalova, L. Roso, R. Fedosejevs, and W. T. Hill, III , Phys. Plasmas **30**, 082110 (2023).
23. S.-Y. Chen, A. Maksimchuk, and D. Umstadter, Nature **396**, 653 (1998).
24. C. Z. He, A. Longman, J. A. Pérez-Hernández, M. de Marco, C. Salgado, G. Zeraouli, G. Gatti, L. Roso, R. Fedosejevs, and W. T. Hill, III, Opt. Express **27**, 30020 (2019).
25. O. Har-Shemesh and A. Di Piazza, Opt. Lett. **37**, 1352 (2012).
26. F. Mackenroth, A. R. Holkundkar, and H.-P. Schlenvoigt, New J. Phys. **21**, 123028 (2019).
27. I. A. Aleksandrov and A. A. Andreev, Phys. Rev. A **104**, 052801 (2021).
28. M. Garten, "Modellierung und validierung von feldionisation in parallelen particle-in-cell-codes", PhD. Thesis (Technische Universität Dresden, 2016).
29. M. V. Ammosov, N. B. Delone, and V. P. Krainov, Proc. SPIE **664**, 138 (1986).
30. N. B. Delone and V. P. Krainov, Phys. Usp. **41**, 469 (1998).
31. H. Burau, R. Widera, W. Hönig, G. Juckeland, A. Debus, T. Kluge, U. Schramm, T. E. Cowan, R. Sauerbrey, and M. Bussmann, IEEE Trans. Plasma Sci. **38**, 2831 (2010).
32. https://www.nist.gov/pml/atomic-spectra-database.
33. B. Shen, Z. Bu, J. Xu, T. Xu, L. Ji, R. Li, and Z. Xu, Plasma Phys. Control. Fusion **60**, 044002 (2018).
34. E. A. Mosman and F. Karbstein, Phys. Rev. D **104**, 13006 (2021).
35. Q. Yu, D. Xu, B. Shen, T. E. Cowan, and H.-P. Schlenvoigt, High Power Laser Sci. Eng. **11**, e71 (2023).
36. N. Ahmadiniaz, C. Bähtz, A. Benediktovitch, C. Bömer, L. Bocklage, T. E. Cowan, J. Edwards, S. Evans, S. Franchino Viñas, H. Gies, S. Göde, J. Görs, J. Grenzer, U. Hernandez Acosta, T. Heinzl, P. Hilz, W. Hippler, L. G. Huang, O. Humphries, F. Karbstein, P. Khademi, B. King, T. Kluge, C. Kohlfürst, D. Krebs, A. Laso-García, R. Lötzsch, A. J. Macleod, B. Marx-Glowna, E. A. Mosman, M. Nakatsutsumi, G. G. Paulus, S. V. Rahul, L. Randolph, R. Röhlsberger, N. Rohringer, A. Sävert, S. Sadashivaiah, R. Sauerbrey, H.-P. Schlenvoigt, S. M. Schmidt, U. Schramm, R. Schützhold, J. P. Schwinkendorf, D. Seipt, M. Šmíd, T. Stöhlker, T. Toncian, M. Valialshchikov, A. Wipf, U. Zastrau, and M. Zepf, arXiv:2405.18063 (2024).

https://doi.org/10.1017/hpl.2025.35 Published online by Cambridge University Press